IEEE Access
Multidisciplinary | Rapid Review | Open Access Journal

Received 1 September 2023, accepted 14 September 2023, date of publication 22 September 2023,
date of current version 3 October 2023.

Digital Object Identifier 10.1109/ACCESS.2023.3318313

RESEARCH ARTICLE

Miniaturized Quad-Port Conformal Multi-Band (QPC-MB) MIMO Antenna for On-Body Wireless Systems in Microwave-Millimeter Bands

MANISH SHARMA[1], (Senior Member, IEEE), PRABHAKARA RAO KAPULA[2], (Member, IEEE), SHAILAJA SALAGRAMA[3], (Member, IEEE), KANHAIYA SHARMA[4], (Member, IEEE), GANGA PRASAD PANDEY[5], (Senior Member, IEEE), DINESH KUMAR SINGH[6], MILIND MAHAJAN[7], (Senior Member, IEEE), AND ANUPMA GUPTA[8]

[1]Chitkara University Institute of Engineering and Technology, Chitkara University, Rajpura, Punjab 140401, India
[2]Department of Electronics and Communication, B. V. Raju Institute of Technology, Narsapur, Telangana 502313, India
[3]Information Technology Program, University of the Cumberlands, Williamsburg, KY 40769, USA
[4]Department of Computer Science and Engineering, Symbiosis Institute of Technology, Symbiosis International (Deemed University), Pune 412115, India
[5]School of Technology, Pandit Deendayal Energy University, Gandhinagar, Gujarat 382007, India
[6]Department of Electronics and Communication Engineering, GL Bajaj Institute of Technology and Management, Greater Noida, Uttar Pradesh 201306, India
[7]Space Applications Centre, ISRO, Ahmedabad, Gujarat 380015, India
[8]Department of Interdisciplinary Courses in Engineering, Chitkara University Institute of Engineering and Technology, Chitkara University, Rajpura, Punjab 140401, India

Corresponding author: Kanhaiya Sharma (sharmakanhaiya@gmail.com)

ABSTRACT In this endeavor, miniaturized quad-port $MIMO_{MB}$ (multiple-input-multiple-output multi-band) antenna with an overall area of 400 mm^2 offering wider-impedance-bandwidth of 8.31GHz-36.14GHz is reported which covers multiple bands including X-band (8.00-12.0 GHz), Ku-band (12.0-18.0 GHz), K-band (18.0-27.0 GHz), partial Ka-band (27.0-40.0 GHz), FR2: n257 (26.50-29.50 GHz), n258 (24.25-27.50) and n261 (27.50-28.35 GHz) is reported for wideband infrastructure. The proposed antenna radiating EM energy is printed on very thin Rogers RTDuroid5880 substrate with thickness 0.254mm. The radiating EM wave patch consists of hexagonal geometry which is etched with a circular-rectangular slot and partial-ground etched by a beveled shape patch for matching of impedance. The conformal capability of the proposed antenna is verified by S-for single-port, dual-port, and proposed four-port antenna. The time-domain analysis confirms the faithful reception of transmitted signals in far-field regions. The diversity performance including ECC_{MB}, DG_{MB}, $TARC_{MB}$, CCL_{MB}, and MEG_{MB} is below permissible standard values with a maximum peak gain of 7.17dBi with stable 2-D radiation patterns in principal planes. The Specific-Absorption-$Rate_{MB}$ (SAR) analysis is carried out at different operating frequencies in Microwave-Millimeter wave bands with SAR $\leq$1.60W/Kg in human phantom tissue and makes it suitable for on-body wireless applications.

INDEX TERMS Conformal MIMO patch, multiband, microwave-millimeter wave bands, thin substrate, ECC_{MB}, DG_{MB}, $TARC_{MB}$, CCL_{MB} and MEG_{MB}, SAR, human phantom tissue.

I. INTRODUCTION

The development of planar technology in the last few decades related to the designing of antennae has been able to attract several researchers. In today's scenario, the motherboard has become very compact thereby reducing the size of the devices. It will be an advantage if the antenna can be more compact, and conformal capability with acceptable Specific-absorption-rate (SAR) that can be used for multiband applications. This literature discusses various microwave-millimeter

The associate editor coordinating the review of this manuscript and approving it for publication was Tutku Karacolak.

This work is licensed under a Creative Commons Attribution-NonCommercial-NoDerivatives 4.0 License.
For more information, see https://creativecommons.org/licenses/by-nc-nd/4.0/

wave application antennae with conformal capabilities and controllable SAR. A compact 28.0GHz antenna with an arc-shaped patch provides an impedance bandwidth of 25.83GHz-30.24GHz [1]. Also, a slotted square patch with an embedded T-shaped stub and defective ground resonates at 28.0GHz with a gain of 11.50dBi and 94% efficiency [2]. Utilizing a two-electromagnetically coupled patch offers a dual band of operation at 38.0GHz and 60.0GHz millimeter-Wave band [3]. A very compact size antenna that resonates at 60.0GHz millimeter-Wave is applicable for body area networks [4] and a genetic-algorithm-based four-band single-port antenna is designed with a population size of 30 with genes in chromosomes equivalent to 36 [5]. A compact antenna [6] for body-centric relay-mode communication is designed for 5.0GHz with high directivity of 7.18dBi. A single-port guitar-shaped patch produces wide operating bandwidth of 2.76GHz-35.93GHz [7], [11], [21], [24] and a low profile two-port dual band is achieved by using a dome-shaped patch with CPW-fees and T-shaped connected stub helps in achieving high isolation [8]. A hexagonal-ring-shaped stub with tapered feed produces dual bands resonating at 28.0GHz/38.0GHz mm-Wave bands [9], [22], [23]. A wide gap between the inter-spaced element of 52.0mm with the combination of circular patch fed by tapered-feed offers more than 10:1 ratio bandwidth between 3.10GHz-20.0GHz [10]. Triple-resonating bands are achieved by utilizing DCOLR (defective-complimentary-open-loop-resonator) which also includes defective feed inclusive of dual-stepped resonator(s) with partial-ground [12]. Better diversity characteristics inclusive of isolation $\geq$16.0dB are achieved in 2-ports UWB-monopole antenna [13], [14]. Four-port MIMO antenna with bandwidth 24.55GHz-26.50GHz is designed for a 24.0GHz center frequency mm-Wave band and the gain is achieved by using a 9×6 circular Split Ring (CSR) [15]. A low-frequency 5G-NR band with four-port accommodates n77, n78, and n79 bands [16], [17], [18], [19]. A super wideband antenna with four notched bands offers operational bandwidth of 1.15GHz-40.0GHz and maintains isolation by arranging the truncated elliptical self-complimentary patch in an orthogonal fashion [20]. 8-port narrow-band (5G applications) [25] and super wideband [26] utilizes flower-shaped patch with side L-shaped stub attached to the ground providing maximum radiation in the desired direction. A review on the conformal antenna is reported [27], [28], [29] which utilizes substrates such as PET, and thin Rogers substrate for bending of antenna applications. A conformal antenna designed on an FR4 substrate utilizes a very thin dielectric thickness of 0.15mm and produces applications within 7.20GHz-9.20GHz [30], [33]. A deployable wearable antenna is modeled on a body with a thickness of skin=2.00mm, fat=4.00mm, and muscle=10.0mm producing a maximum specific-absorption rate of 0.512 W/Kg at 2.45GHz [31]. A breast-cancer antenna is capable of detecting tumors which is traceable between a bandwidth of 8.50GHz-10.50GHz [32], [34]. A detailed investigation of SAR and thermal effects is studied by using patch-antenna when deployed on the body and also checking on the fabric-cotton wearable applications with antenna providing resonance at 1.80GHz, 2.40GHz, and 5.00GHz and 8.90GHz. Classical theory of characteristics modes is applied on conformal MIMO antenna which is designed in accordance with the electromagnetic properties of the implantable antenna with I-type patches between dual-radiators and slot-structure in ground achieving good isolation [37]. Utilizing partially reflecting-surface with Dielectric-Resonator-Antenna (DRA) improves the gain of the antenna [38], [39].

In this work, a slotted hexagon patch-geometry in combination with beveled ground below the patch forms wideband antenna with multi-band applications designed and analyzed on low permittivity 2.20 flexible substrate. The single-antenna is transformed to two-port and four-port MIMO configuration for higher data rate of transmission with reduction of fading. The calculated SAR at different resonance confirms the value below 1.60 W/Kg make it more feasible for wearable and hand-held devices. The detailed study is discussed in the sections given below

II. CONFORMAL ANTENNA

Wireless communication has emerged as an impressive technology that has developed to a large extent in delivering data with higher data rates and low latency through the implementation of 5G technology. A multiband antenna is desirable with very compact which can be useful for multiple-wireless applications. In achieving the above objective with multiple bands embedded in single-antenna, an ultra-compact antenna is proposed with inheriting the capability of conformal characteristics which can be used for wearable devices, and the design methodology with supporting results is discussed below

A. SINGLE-PORT CONFORMAL ANTENNA

Details of the multiband-antenna$_{MB}$ are depicted in Fig. 1 shows which is printed on a thin RogersRT^{TM} Duroid dielectric. The top plane of the dielectric is printed with a radiator patch which is connected to a 50Ω-microstrip feedline with an overall antenna dimension of $L_{sub} \times W_{sub} \times t_{sub}$ mm^3. The designed radiator which is capable of generating wider impedance-bandwidth is united with optimized feed and is connected to matched SMK2.92mm connector manufactured by Jhonson with manufacturer part no. 145-0711-812 for signal input between 5.0GHz-40.0GHz. The opposite plane is printed with fractal-ground with a bent slot to achieve wider impedance bandwidth with the matching of impedance as shown in Fig. 1(a). Fig. 1(b) illustrates the front view of the slotted-hexagonal radiator which consists of a polygon shape with side-length L_p mm. The radiating patch is carved with a circular slot of radius R_s (in mm) and a trapezoidal slot of area $((S_1+S_3)/2 \times S_2)$ mm. On the opposite face of the dielectric, partially-imprinted ground includes a beveled-shaped slot as observed in Fig. 1(c). The partial ground occupies an area

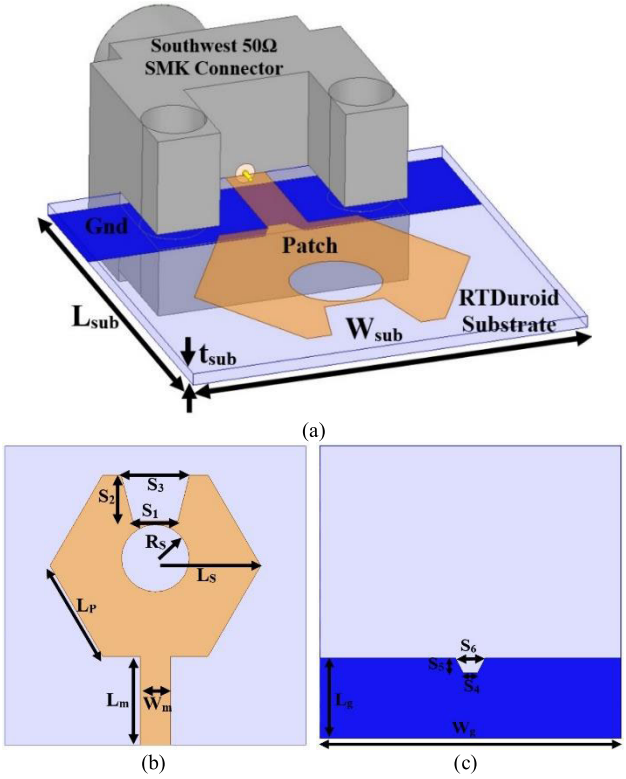

FIGURE 1. Proposed Conformal 1-Port Antenna (a) Isometric (b) Radiating Patch view (c) Ground view.

TABLE 1. Optimal values tabulated from Fig. 1.

Single Port					
Dimension	**mm**	**Dimension**	**mm**	**Dimension**	**mm**
L_{sub}	10.0	W_{sub}=W_g	10.0	t_{sub}	0.254
L_m	2.75	W_m	0.80	L_p	3.75
R_s	1.25	L_s	3.75	S_1	2.20
S_2	1.30	S_3	1.25	S_4	0.40
S_5	0.75	S_6	0.50	L_g	2.50
Dual Port					
Dimension	**mm**	**Dimension**	**mm**	**Dimension**	**mm**
W_{g1}	20.0	L_{g1}	10.0	K	9.00
S_L	7.50	S_W		0.50	
Four Port					
Dimension	**mm**	**Dimension**	**mm**	**Dimension**	**mm**
L_{g2}	20.0	W_{g2}	20.0	K	**9.00**

of $L_g \times W_g$ mm^2 and gap (L_m-L_g) mm is responsible for -10dB wide operational bandwidth. The optimal dimensions extracted from the EM-simulation Ansys HFSS are recorded in Table 1 given below (Fig. 1)

B. EVOLUTION

Fig. 1 antenna is achieved by carrying out several iterations and resulting in an optimal version. However, the evolution of the final version of the single-element is obtained by four iterations and the respective antenna is named Ant. A_1, Ant. A_2, Ant. A_3 and Ant. A_4 respectively. Ant. A_1 as shown in Fig. 2(a) is printed with a polygon patch and partial-rectangular ground on respective opposite planes.

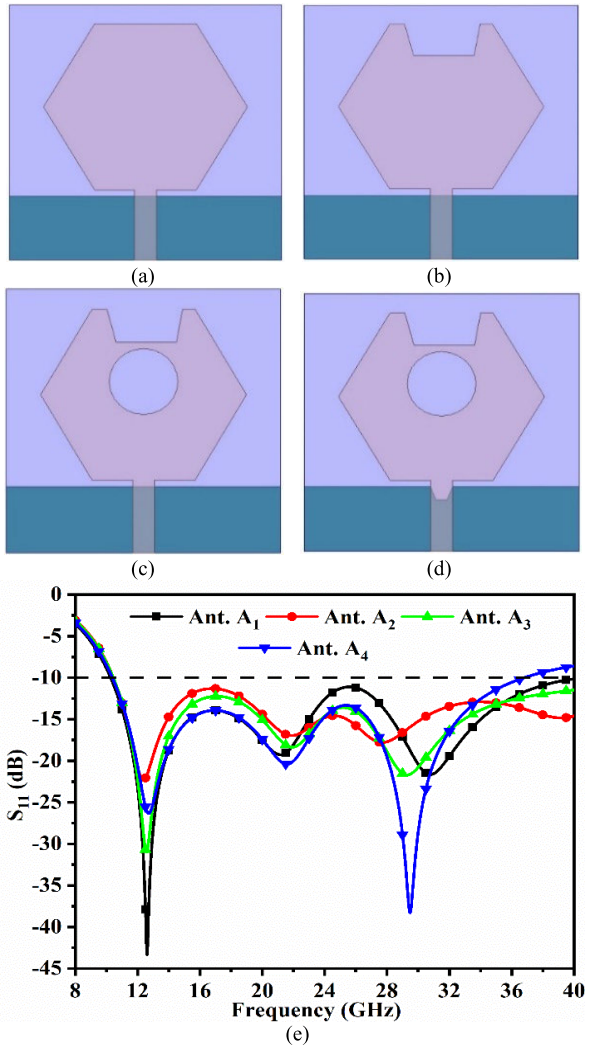

FIGURE 2. Configuration of Single-Port Conformal (a) Ant. A_1 (b) Ant. A_2 (c) Ant. A_3 (d) Ant. A_4 (e) S_{11} result of Ant. A_1-Ant. A_4.

The polygon patch with side L_p mm is calculated by following equations [40]

$$L_p = \frac{c}{4 \times f}\sqrt{1/(1+\varepsilon_{eff})} \tag{1}$$

where c (c=3 × 10^8 m/s: the light speed with vacuum as a medium), f is the center design frequency in GHz, and ε_{eff} is the effective permittivity which is calculated from Equation 2 given below [40]

$$\varepsilon_{eff} = \frac{\varepsilon_r + 1}{2} + \frac{\varepsilon_r - 1}{2}\left[1 + \frac{12 \times t_{sub}}{W_m}\right]^{\frac{1}{2}} \tag{2}$$

This iteration provides the impedance bandwidth of 10.28GHz-40.0GHz but with a considerably acceptable matching of impedance. Further, the polygon patch is etched by the slot of the area given by following Equation 3

$$\left(\frac{S_1 + S_3}{2}\right) \times S_2 = \left(\frac{2.20 + 1.25}{2}\right) \times 2.75 = 4.74\,mm^2 \tag{3}$$

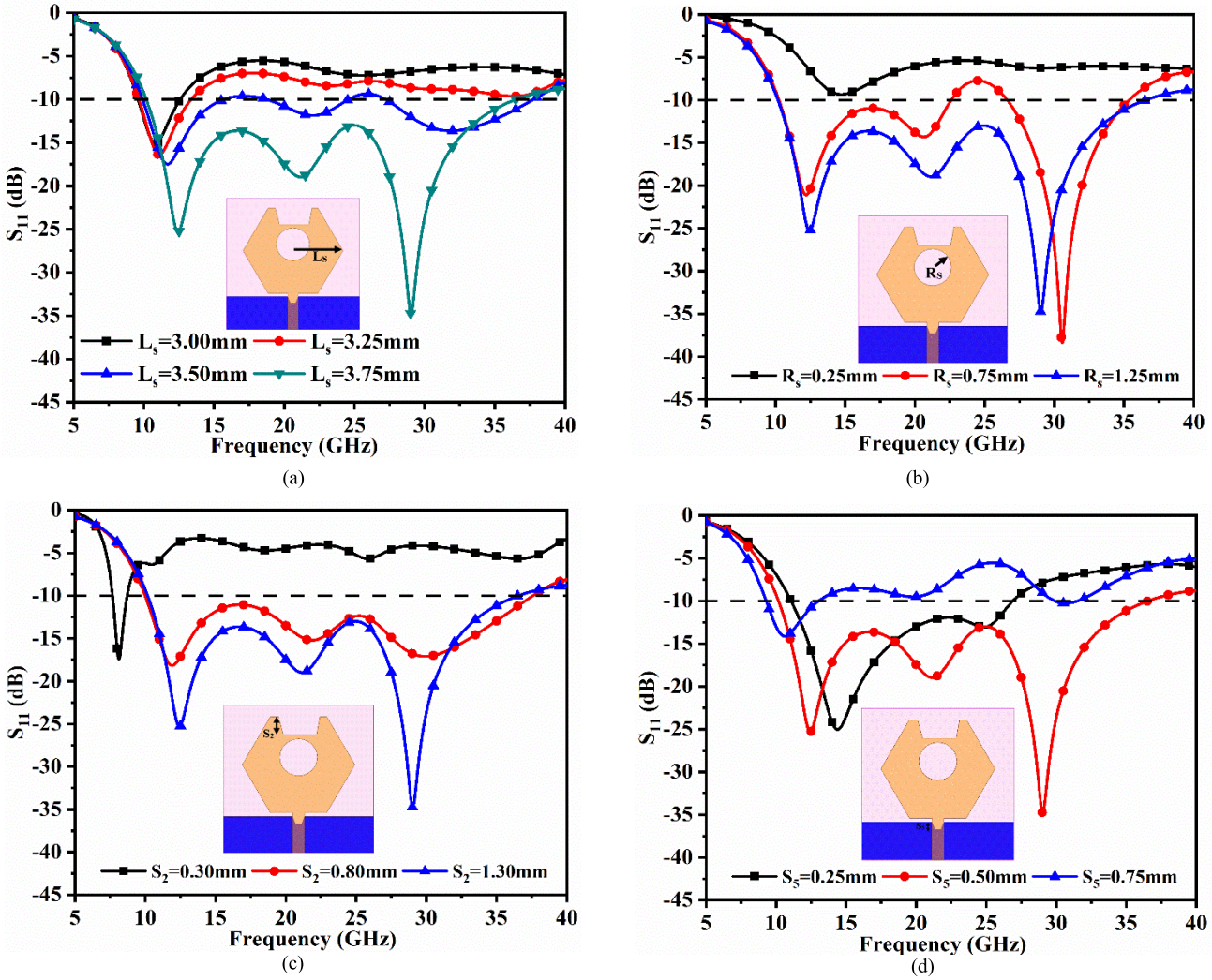

FIGURE 3. Parametric Study of key parameter (a) L_S (b) R_S (c) S_2 (d) S_5.

Which helps in improving the operating bandwidth and provides single-resonance at 12.36GHz with $S_{11} = -22.29$dB. The third iteration is the addition of a circular slot with a radius Rs mm on the radiating patch (Ant. A_3) helps in improving the matching of impedance at resonance 12.56GHz ($S_{11} = -30.97$dB) and 29.17GHz ($S_{11} = -21.67$dB) respectively. The final version of the single-port antenna is achieved by etching a beveled-shaped slot in the ground with an impedance bandwidth of 10.38GHz-36.79GHz. This version of the proposed antenna, however, the Ant. A4 which is the final version of the proposed antenna, offers better impedance matching beyond 23GHz with marginally reduced bandwidth at higher cut-off frequency and does not affect the design objective. With three resonances within the impedance bandwidth and are centered at 12.71GHz ($S_{11} = -26.34$dB), 21.58GHz ($S_{11} = -20.41$dB), and 29.48GHz ($S_{11} = -38.30$dB).

C. PARAMETRIC STUDY

The final version of the mono-radiator represented by Fig. 1 which is optimized, is achieved by changing the different values of the dimension.

This is done by applying parametric variation to a key parameter such as L_s (radius of equivalent circle encircling the polygon patch), Rs (etched circular slot on the patch), S_2 (height of etched trapezoidal slot), and S5 (height of the etched-beveled slot in the ground). The parameter L_s (in mm) which is the equivalent radius of the hexagon patch encircling it is changed from 3.00mm to 3.75mm with step size $\Delta L_s = 0.25$mm. The value of $L_s = 3.00$mm, which signifies the smaller area of the radiating patch offers narrow bandwidth of 9.59GHz-12.59GHz with resonance centered at 10.83GHz. Further increase in values of L_s at 3.25mm and 3.50mm helps in improving the matching of bandwidth. For the optimized value of $L_s = 3.75$mm, the bandwidth of 26.41GHz is

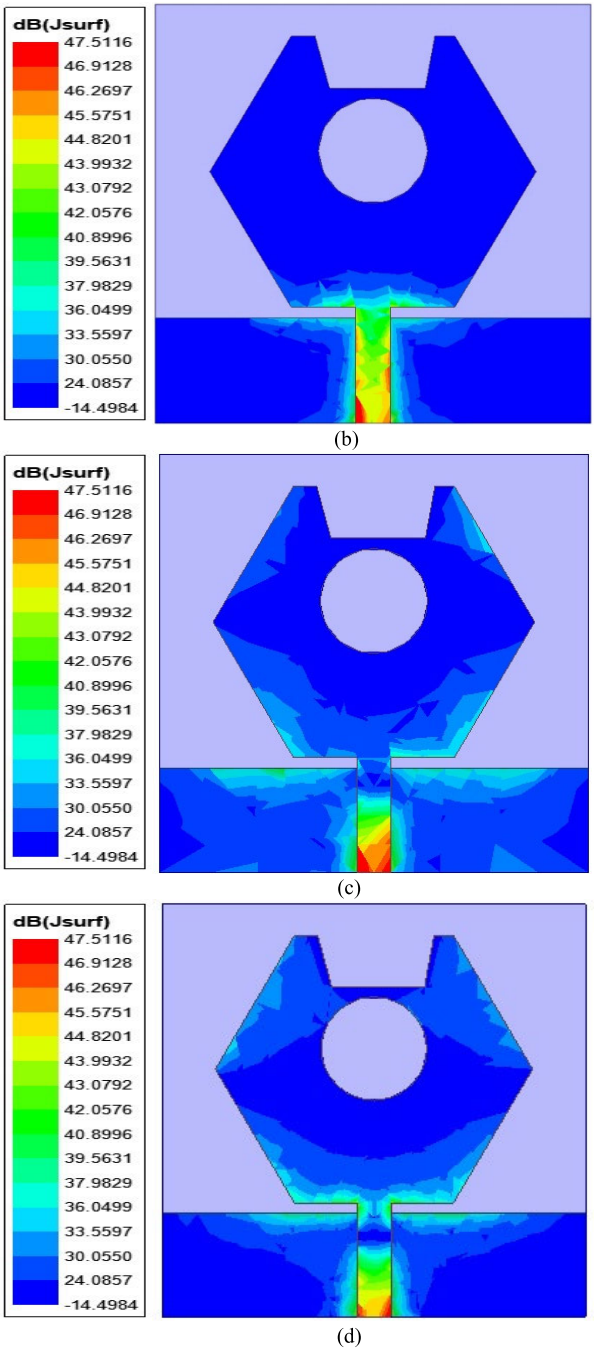

FIGURE 4. Surface-Current-Density distribution at (a) 12.40GHz (b) 24.0GHz (c) 28.0GHz.

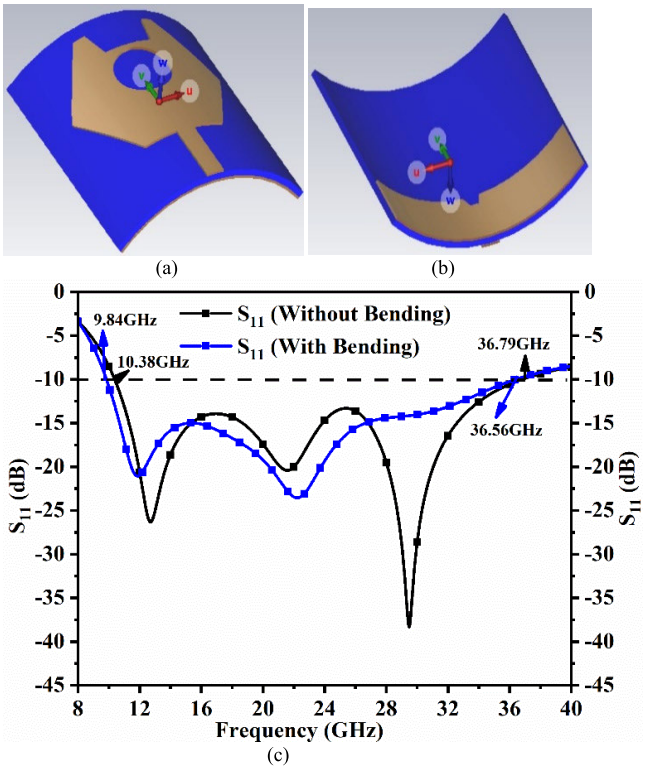

FIGURE 5. Conformal capability of single-port antenna (a) Bend with a front view (b) Bend with a ground view (c) Comparison of S-parameter.

obtained. The second key parameter Rs, which is an etched circular slot on a polygon patch observes a large swing of the S_{11} bandwidth for values of Rs between 0.25mm to 1.25mm. The lower values of R_s observe the narrow bandwidth but for Rs=1.25mm, the objective of large-bandwidth multi-band applications is achieved as shown in Fig. 3(b) another important parameter, S_2 which is the height of the trapezoidal slot etched on top of hexagonal-patch, observes improved impedance-bandwidth with the value of S_2 from 0.30mm to 1.30mm. Good matched-impedance bandwidth is achieved for $S_2 = 1.30$mm. The beveled slot in the rectangular ground with a height of $S_5 = 0.75$mm achieves the highly matched impedance-bandwidth and the remaining values of $S_5 = 0.25$mm and 0.50mm are discarded.

D. IMPEDANCE GRAPH, SURFACE-CURRENT-DENSITY-DISTRIBUTION, CONFORMAL CHARACTERISTICS

Fig. 4(a)-(c) shows the distribution of SCD_{MB} for the frequency values corresponding to 12.40GHz, 24.0GHz, and 28.0GHz respectively. In all three cases, it can be concluded that maximum SCD_{MB} is concentrated within the microstrip feed line which forms the bridge of transmission of a signal from the input port to the radiating patch. This indicates that at these frequency values, all the signal is fed to the radiating patch and the patch radiates the input signal rather than storing it. Thus, the correlation between the net impedance and radiation characteristics is easily established at these frequency values providing high gain and efficiency.

The proposed single-port antenna discussed occupies the wider-impedance bandwidth with multiple-band including X-band, 24.0GHz, and 28.0GHz bands. The proposed work utilizes a thin Rogers-Dielectric with a thickness of 0.254mm and can be easily useable for conformal applications regardless of whether the bandwidth should not be compromised. Fig. 5 shows the conformal configuration with Fig. 5(a)

representing bent at 45° with front and ground view. The planar antenna (without bending) occupies an impedance bandwidth of 10.38GHz-36.79GHz and with bending corresponds to $|S_{11}| < -10.0dB$ bandwidth of 9.84GHz-36.43GHz, thereby, the operating impedance bandwidth is not compromised and can be easily integrated for wearable multiband-applications.

III. DUAL AND FOUR-POT CONFORMAL MIMO ANTENNA

Section II has seen the analysis of a single-port conformal antenna producing wide impedance bandwidth of 10.0GHz-39.38GHz without bending of the antenna at and 10.0GHz-36.56GHz with conformal capability at 45°. However, when they are deployed in a live wireless communication application environment, will suffer from multiple-path fading of the transmitted signals and hence, the distorted pulse will be received. This effect also reduces the efficiency which will decrease the working bandwidth. To improve the bandwidth and to control multiple-path fading, multiple-radiating elements achieving several diversity schemes such as spatial, radiation, or polarization diversity need to be implemented while designing multiple-input-multiple-output antenna (MIMO) configuration. The MIMO configuration will enhance the bandwidth and ensures the receiving of the signal efficiently when the signal impinges at any angle on the receiver antenna. The Shannon-Hartley theorem on channel capacity is given by [41]

$$Ch.Cap._{M\times S} = D_{M\times S}\Delta B\, log_2(1+\frac{S}{N}) \qquad (4)$$

where $Ch.Cap._{M\times S}$ is the Channel-Capacity (CC) given by b/s/Hz, ΔB is the matched operational bandwidth, $D_{M\times S}$ is the integral multiple factors for MIMO configuration and corresponds to the ratio between the signal and the additional noise (S/N). Additional radiators forming $MIMO_{MB}$ configuration also ensure the enhancement of channel capacity thereby reducing multi-path fading issues.

Fig. 6 shows the two-port conformal MIMO antenna configuration which will reduce not only multi-path fading effects but also preserves the required impedance bandwidth for multi-band applications. Fig. 6(a) shows the simulation configuration of the conformal antenna with the bent of 45° angle and Fig. 6(b) corresponds to reflection and transmission coefficients.

As per the observations, the proposed conformal antenna maintains a bandwidth of 10.12GHz-36.10GHz (S_{11}) for radiator 1 and 8.06GHz-35.76GHz (S_{22}) for radiator 2.

The MIMO configuration is obtained by placing the identical modified slotted hexagon patch orthogonally with respective partial rectangular ground connected with a thin stub of dimension 7.5mm×0.50mm. Fig. 6(b) also shows the transmission coefficient or isolation between the two ports with isolation being more than 17.50dB (S_{12}, S_{21}) for both radiating elements. Fig. 6(c)-(d) shows the distribution of current density on the surface for un-connected and connected ground. In both cases, the required isolation is maintained and the antenna radiates efficiently. However, there is a need for common ground in MIMO-antenna configuration [35]

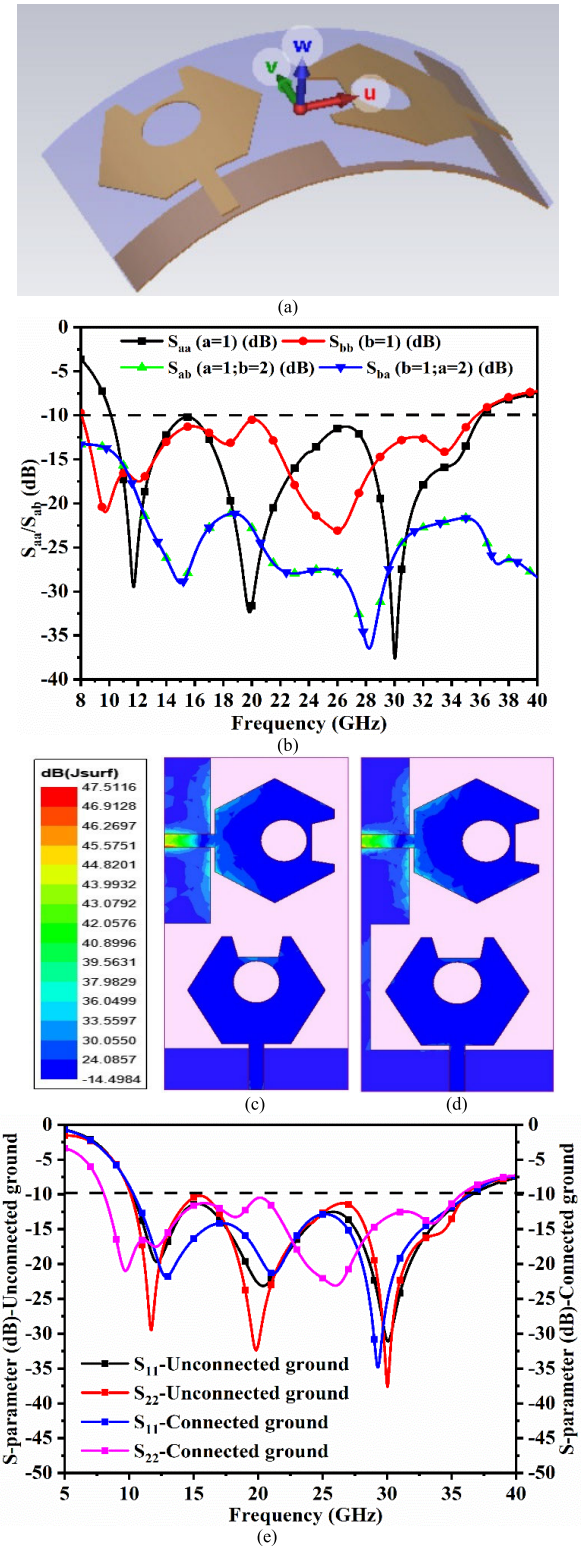

FIGURE 6. Conformal capability of dual-port antenna (a) Bend capability (b) S-parameter; Surface-current distribution at 28.0GHz (c) Unconnected ground (d) Connected ground (e) S-parameter: Unconnected and Connected ground.

TABLE 2. S-parameter comparison Fig. 6(e).

S-parameter (dB)	Unconnected Ground Bandwidth (GHz)	Connected Ground Bandwidth (GHz)
S_{11}	10.23-36.61	10.12-36.11
S_{22}	10.35-36.43	8.06-35.76

because the signal needs to have a common-ground plane which helps in interpreting all the levels of signal properly based on the reference-zero ground level. Fig. 6(e) shows the comparison of S-parameter graph of MIMO antenna configuration with unconnected and connected ground. The impedance bandwidth in both the cases is tabulated in Table 2 given below.

In both the cases, the MIMO antenna configuration covers the required multi-band applications bandwidths.

The proposed two-port MIMO antenna provides wide-impedance bandwidth and hence, the transmission of signal at this bandwidth needs to be evaluated which is carried out by studying time-domain performance. Fig. 7 shows the evaluation of the time-domain performance of the MIMO antenna when subjected to pulse as the input. The simulation environment is set up with identical MIMO antenna placed in face-to-face and side-to-side orientations as shown in Fig. 7(a)-(b). The minimal distance of 300mm is maintained to ensure the far-field condition given by [40]

$$\textit{Far Field region} > \frac{2 \times 2 \times w_{SUB}^2}{\lambda_C} \tag{5}$$

where $2 \times W_{wub} = 20.0$mm is the maximum dimension of the antenna and λ_C is the cut-off frequency in GHz.

$$\phi = -\frac{d\theta(\omega)}{d\omega} \tag{6}$$

$$\rho = max_{\phi}\left[\frac{\int S_{Tx}(t)\, S_{Tx}(t-\phi)dt}{\sqrt{S_{Tx}^2(t)\,dt}\sqrt{S_{Rx}^2(t)\,dt}}\right] \tag{7}$$

Fig. 7(c) shows the graph of group delay which is calculated by Equation 6. The group delay in general is used to study the time response between two antenna systems and is the measure of the delay in received signal concerning phase distortion.

This ensures that the received signal shape of the transmitted pulse is preserved without much pulse distortion. The group delay as observed in Fig. 7(c) notes the variation between ± 0.1ns which satisfies the ideal condition. Fig. 7(d) shows the impulse response of the MIMO-antenna in both orientations. It can be observed that the face-to-face and side-to-side received pulses overlap without distortion in comparison to the input impulse. However, there are additional harmonics with very low amplitude that can be easily suppressed at the receiver. Also, the received signal strength (mV) can be easily increased by the integration of a low-noise amplifier.

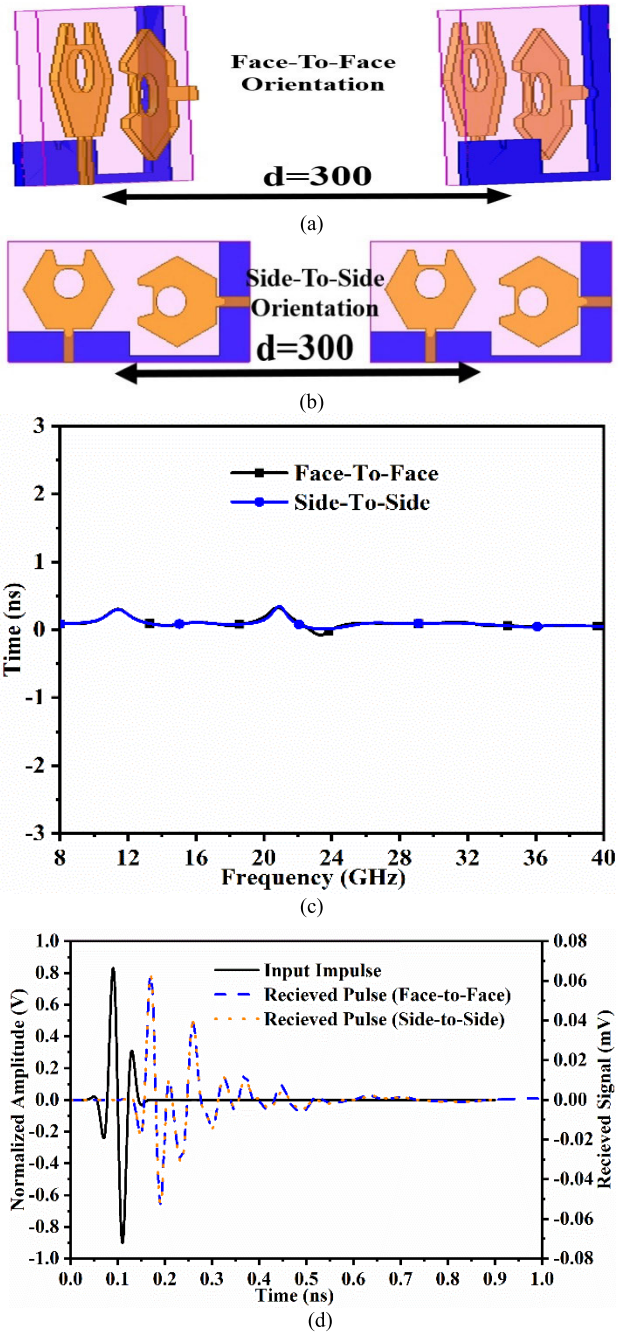

FIGURE 7. Time-domain analysis (a) Face-to-Face alignment (b) Side-to-Side alignment (c) Group delay (d) Impulse response.

The advantage of transforming single-port to two-port MIMO configuration with common connected ground is studied which reduces the multi-path fading. The increase in the number of radiating elements in the MIMO configuration from 2-Port to 4-Port will further enhance the reduction in fading of the signal. Fig. 8 shows the four-port configuration of the MIMO antenna. Fig. 8(a)-(c) shows the Isometric and transparent front view of the proposed work where all the radiating antennae are connected to

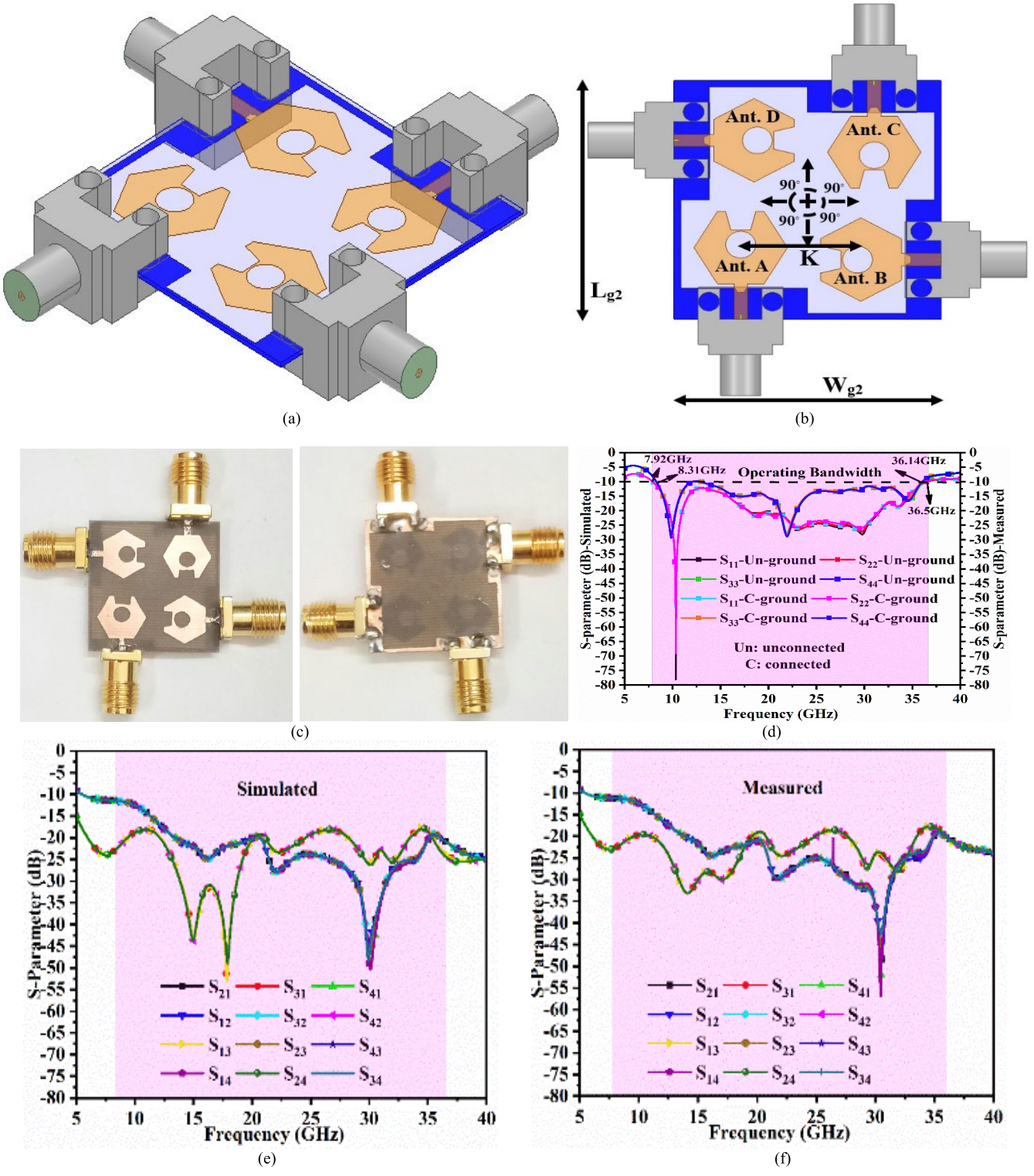

FIGURE 8. Four port MIMO configuration (a)-(b) Perspective and transparent front view with printed radiating patch and ground in the simulation environment (c) Fabricated prototype (d) Simulated and Measured reflection coefficient (e)-(f) Simulated and Measured transmission coefficient.

modeled SMK2.92mm connector for signal input. The radiating elements are aligned orthogonally (90° with each other) and spacing of K=9.00mm between them to ensure proper isolation. Fig. 8(c) shows the developed prototype by a conventional method with fine-quality substrate and connectors to achieve accurate results. Fig. 8(d) records the simulated and measured reflection coefficients with a shaded portion indicating the operating bandwidth.

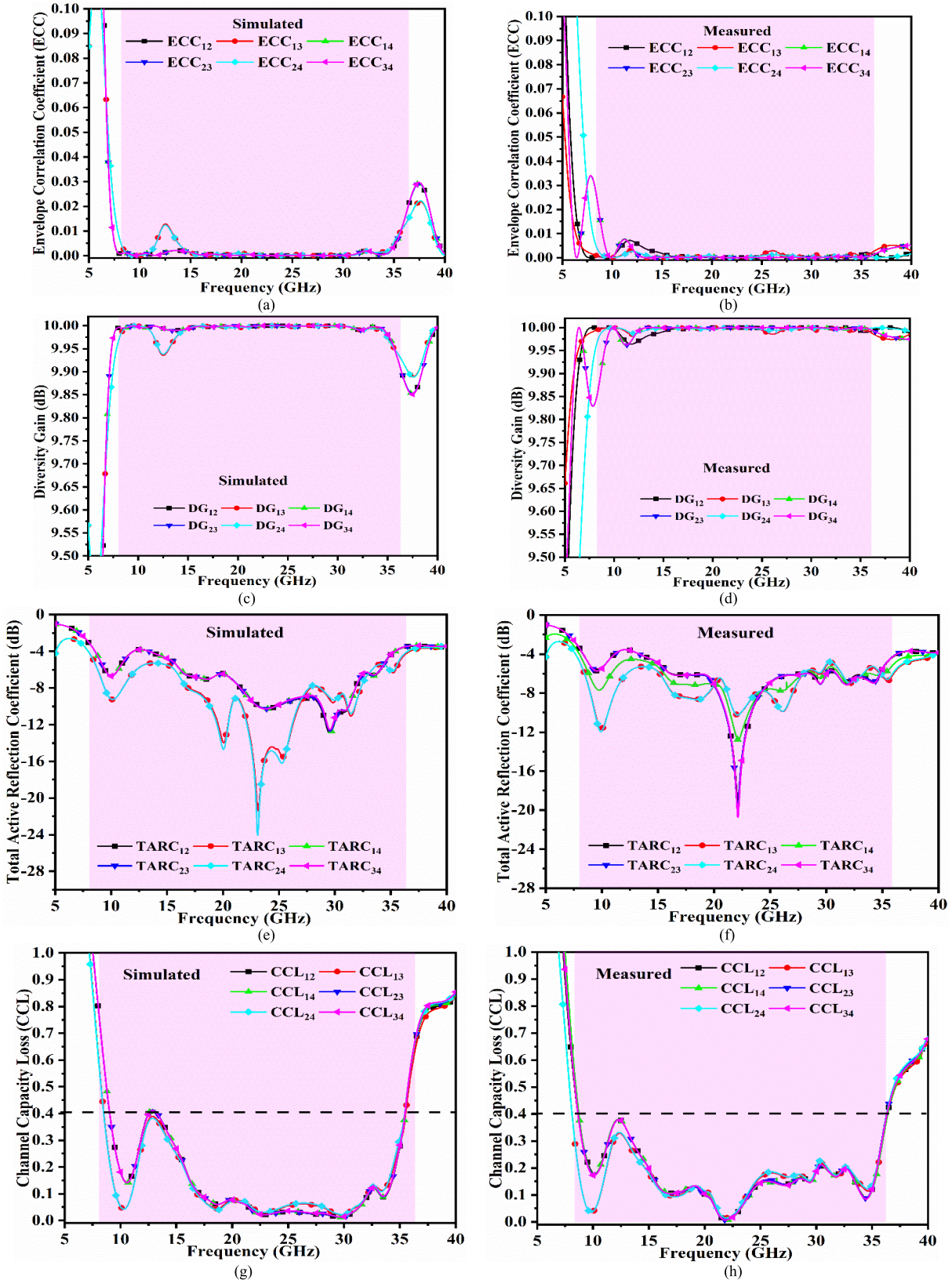

FIGURE 9. Four port MIMO configuration with simulated and measured diversity parameters (a)-(b) Simulated and measured ECC_{2-Port} (c)-(d) Simulated and measured DG_{2-Port} (e)-(f) Simulated and measured $TARC_{2-Port}$ (g)-(h) Simulated and measured CCL_{2-Port} (i)-(k) Simulated MEG_{12}, MEG_{13}, MEG_{14} (l)-(n) Measured MEG_{12}, MEG_{13}, MEG_{14}(o)-(q) Simulated MEG_{23}, MEG_{24}, MEG_{34} (r)-(t) Measured MEG_{23}, MEG_{24}, MEG_{34}.

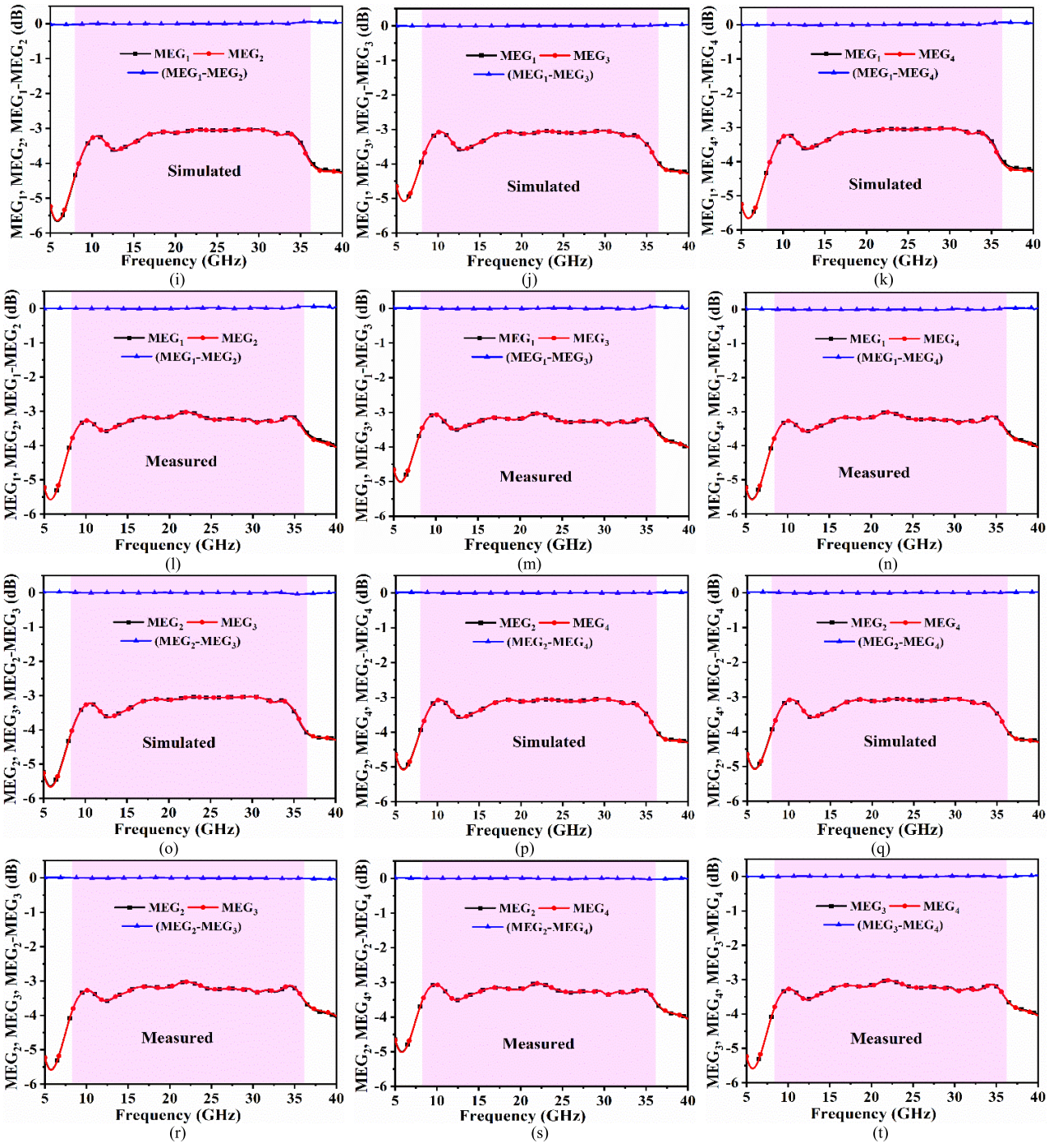

FIGURE 9. *(Continued.)* **Four port MIMO configuration with simulated and measured diversity parameters (a) -(b) Simulated and measured ECC_{2-Port} (c)-(d) Simulated and measured DG_{2-Port} (e)-(f) Simulated and measured $TARC_{2-Port}$ (g)-(h) Simulated and measured CCL_{2-Port} (i)-(k) Simulated MEG_{12}, MEG_{13}, MEG_{14} (l)-(n) Measured MEG_{12}, MEG_{13}, MEG_{14}(o)-(q) Simulated MEG_{23}, MEG_{24}, MEG_{34} (r)-(t) Measured MEG_{23}, MEG_{24}, MEG_{34}.**

The simulated bandwidth corresponds to 7.92GHz-36.50GHz and the measured bandwidth is 8.31GHz to 36.14GHz. Fig. 8(e)-(f) corresponds to the simulated and measured transmission coefficient with isolation of more than 12.50dB in a simulation environment and more than 15.0dB for measured values. The simulation environment provides exact 50Ω matching between the port and the feedline. Also, the finite-element-method (FEM) do provide good approximation calculation of maxwell's equations. Whereas, in measurement conditions, the quality of SMK connector used, quality of the substrate, precision in calibration of VNA with accuracy in measurement are the few factors which results in deviation of S-parameter in comparison of the simulation results.

IV. DIVERSITY PERFORMANCE AND FAR-FIELD RESULT DISCUSSION COMPARISON OF PRESENT STATE-OF-THE-ART MIMO ANTENNA

The single-port multiband antenna in the proposed work with conformal capability exhibits good far-field results and occupies multi-band bandwidth which finds applications in several wireless applications. However, when the radiating patch is increased in number say d×k with d=1,2,3,4 and k=1,2,3,4 offers the following s-matrix with 16-S-parameters given below [41]

$$[\boldsymbol{S}] = \begin{bmatrix} \boldsymbol{S_{11}} & \boldsymbol{S_{12}} & \boldsymbol{S_{13}} & \boldsymbol{S_{14}} \\ \boldsymbol{S_{21}} & \boldsymbol{S_{22}} & \boldsymbol{S_{23}} & \boldsymbol{S_{24}} \\ \boldsymbol{S_{31}} & \boldsymbol{S_{32}} & \boldsymbol{S_{33}} & \boldsymbol{S_{34}} \\ \boldsymbol{S_{41}} & \boldsymbol{S_{42}} & \boldsymbol{S_{43}} & \boldsymbol{S_{44}} \end{bmatrix} \tag{8}$$

The S-parameter shown in the above matrix corresponds to reflection coefficients (S_{11}, S_{22}, S_{33} S_{44}) and transmission coefficients (S_{12}, S_{13}, S_{14}, S_{21}, S_{23}, S_{24}, S_{31}, S_{32}, S_{34}, S_{41}, S_{42}, S_{43}). The above S-parameters need to maintain the required bandwidth (S_{aa}; a=1,2,3,4) and minimum required isolation (S_{ab}; a=1,2,3,4; b=1,2,3,4). When the input signal is fed to the antenna. Due to the property of radiating os signals, the inter-radiating signals need to be isolated from each other to avoid destructive interference, and hence, the parameter related to diversity performance known as Envelope-Correlation-Coefficient$_{MB}$ (ECC_{MB}; MB-multiband) needs to be calculated. The modulus values of ECCMB vary between 0 and 1 with 0 indicating nill interference of radiation between inter-spaced elements and 1 with higher interference. The ECC_{MB} for a four-port MIMO configuration is evaluated either by radiation pattern or by extracted S-parameters. Equation 9-Equation 14 shows the calculation of ECCMB by using the radiation pattern method considering the m^{th} and s^{th} port in the MIMO configuration [41], (9), as shown at the bottom of the page, where $\gamma_m^2\gamma_s^2$ signifies the variance of corresponding ports and mathematically is written by following sets of equations Mathematically [41]

$$\int_0^{2\pi}\int_0^{\pi} \left(\left(XPRG_{\theta.m}(\theta,\phi)\,P_\theta(\theta,\phi) + G_{\phi.m}(\theta,\phi)\,P_\phi(\theta,\phi)\right)\right) \tag{10}$$

$$G_{\theta m}(\theta,\phi) = E_{\theta m}(\theta,\phi)\,E^*_{\theta s}(\theta,\phi) \tag{11}$$

$$G_{\phi m}(\theta,\phi) = E_{\phi m}(\theta,\phi)\,E^*_{\phi s}(\theta,\phi) \tag{12}$$

$$G_{\theta s}(\theta,\phi) = E_{\theta s}(\theta,\phi)\,E^*_{\theta m}(\theta,\phi) \tag{13}$$

$$G_{\phi s}(\theta,\phi) = E_{\phi s}(\theta,\phi)\,E^*_{\phi m}(\theta,\phi) \tag{14}$$

where $E_{\theta m}$, $E_{\phi m}E_{\theta s}$ and $E_{\phi s}$ are complex-electric fields with (θ, ϕ) for the m_{th} and s_{th} antenna respectively. The ECC values are real values which are plotted in Figure 9(a)-(b) showing the amplitudes of the signals at antennas and in the Rayleigh fading channel, the amplitude of the envelope correlation coefficient is given by [41]

$$\rho_e = |\rho_c|^2 \tag{15}$$

The ECC can be calculated from 3-D radiation and S-parameters. Assuming a uniform multipath environment the ECC_{MB} is evaluated from the following Equations using S-parameters [41]

$$ECC = \rho_e(m,s,N) = \frac{\left|\sum_{n=1}^{N} S^*_{m,n}S_{n,s}\right|^2}{\pi_{k=(m,s)}\left[1-\sum_{n=1}^{N} S^*_{m,n}S_{n,k}\right]} \tag{16}$$

where $\rho_e(m,s,N)$ is the ECC_{MS} between the m_{th} and s_{th} port of the N-Element system. The ECC_{MB} for any two-port MIMO network is given by [41]

$$ECC_{MB} = \frac{\left|S^*_{mm}S_{ms} + S^*_{sm}S_{ss}\right|^2}{\left(1-|S_{ii}|^2-|S_{sm}|^2\right)\left(1-|S_{ss}|^2-|S_{ms}|^2\right)} \tag{17}$$

And for two-port and four-port, ECC_{MB} is given by

$$ECC_{MB(TwoPort)} = \frac{\left|S^*_{11}S_{12} + S^*_{12}S_{22}\right|^2}{\left(1-|S_{11}|^2-|S_{21}|^2\right)\left(1-|S_{12}|^2-|S_{22}|^2\right)} \tag{18}$$

$$ECC_{MB(FourPort)} = \frac{\left|S^*_{11}S_{12} + S^*_{12}S_{22}+S^*_{13}S_{32} + S^*_{14}S_{42}\right|^2}{\left(1-|S_{11}|^2-|S_{21}|^2-|S_{31}|^2-|S_{41}|^2\right)\left(1-|S_{12}|^2-|S_{22}|^2-|S_{32}|^2-|S_{42}|^2\right)} \tag{19}$$

The ideal value of ECC_{MB} is 0 indicating the independent working of the antenna radiating elements and the standard or acceptable values are $ECC_{MB} \leq 0.50$. The exact values of ECC are evaluated using far-field patterns but due to resource limitations, the ECC_{MB} in the proposed work is evaluated by Equation (18) for two-port and Equation 19 for four-port. The ECC_{MB} (m,s) MIMO configuration with m=1,2,3,4 and s=1,2,3,4, ECC_{12}, ECC_{13}, ECC_{14}, ECC_{23}, ECC_{24}, and ECC_{34} are calculated for both simulated and measured as shown in Fig. 9(a)-(b). The simulated values of ECC_{MB} are below 0.40 and for measured these values fall below 0.30 satisfying well the ideal value condition $ECC_{MB} \leq 0.50$. Equation 18 & Equation 19 fulfills the requirement of evaluation of ECC_{MB} by assuming the antennas have higher

$$\gamma_c = \frac{\int_0^{2\pi}\int_0^{\pi}\left(\left(XPRE_{\theta.m}(\theta,\phi)\,E^*_{\theta,s}(\theta,\phi)\,P_\theta(\theta,\phi) + E_{\phi.m}(\theta,\phi)\,E^*_{\phi,s}(\theta,\phi)\,P_\phi(\theta,\phi)\right) sin\theta d\theta d\phi}{\sqrt{\gamma^2_m}\sqrt{\gamma^2_s}} \tag{9}$$

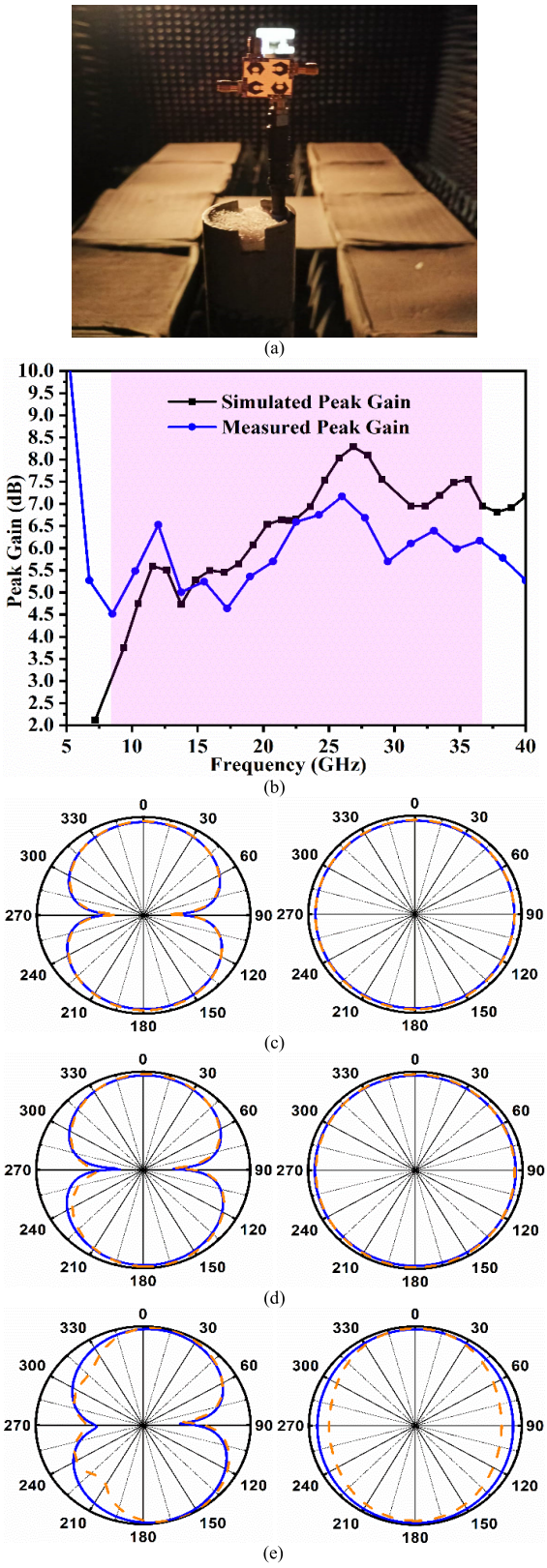

FIGURE 10. (a) Photograph of proposed MIMO antenna placed within ANECHOIC CHAMBER (b) Simulated & Measured peak gain; simulated and measured 2-D radiation pattern at (c) 11.0GHz (d) 15.0GHz (e) 20.0GHz (f) 24.0GHz (g) 28.0GHz (h) 30.0GHz (i) Simulated and measured radiation efficiency.

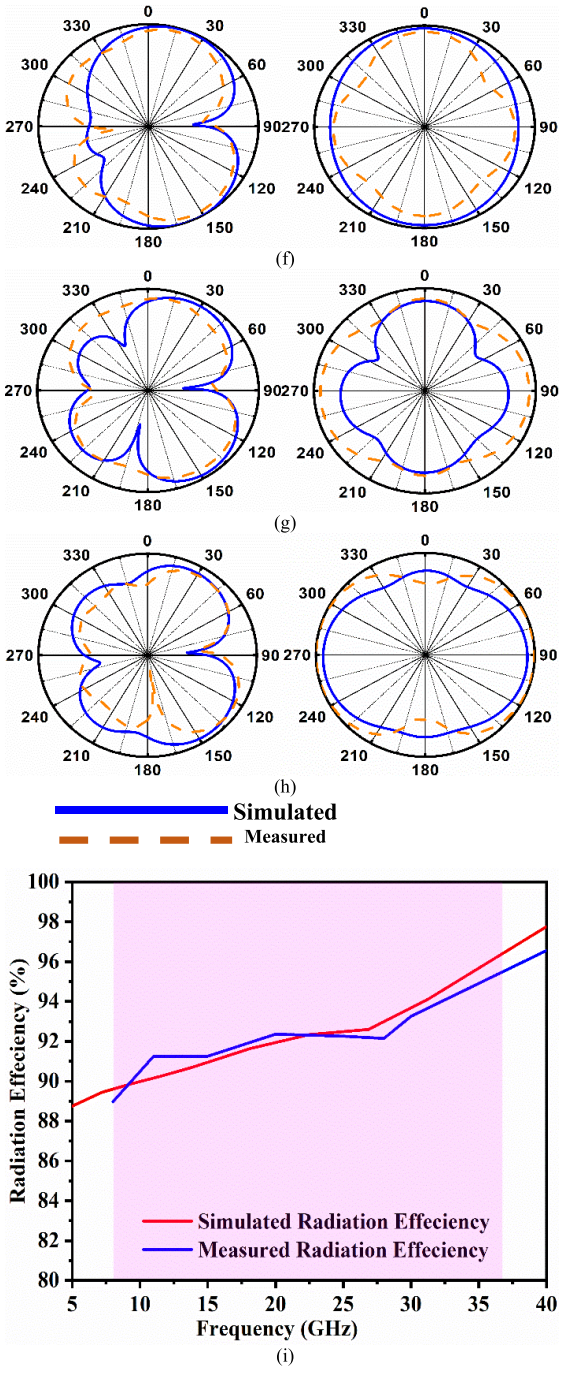

FIGURE 10. *(Continued.)* (a) Photograph of proposed MIMO antenna placed within ANECHOIC CHAMBER (b) Simulated & Measured peak gain; simulated and measured 2-D radiation pattern at (c) 11.0GHz (d) 15.0GHz (e) 20.0GHz (f) 24.0GHz (g) 28.0GHz (h) 30.0GHz (i) Simulated and measured radiation efficiency.

efficiencies and no mutual-coupling losses, uniform multi-path environment and the load termination of the antenna is 50Ω.

The Diversity-Gain$_{MB}$(DG$_{MB}$) is calculated to quantify the performance characteristics of the diversity scheme used (spatial, polarization, or radiation diversity). The DG$_{MB}$ is

related to ECC_{MB} by the following formula [41]

$$DG_{MB} = 10\sqrt{1 - |\rho_e|^2} \tag{20}$$

The DG_{MB} values as per the standard values are $DG_{MB} \geq 9.95dB$. Fig. 9(c)-(d) shows the calculated values of DG_{MB} for both simulated & measured s-parameters with values corresponding to more than 9.95dB and 9.9999dB respectively. The radiation efficiencies and the operating bandwidth of the $MIMO_{MB}$ cannot be accurately calculated by S-parameters (reflection and transmission coefficients). Thus, the coupling and the random-signal combination are calculated by Total Active Reflection $Coefficient_{MB}$ ($TARC_{MB}$) which gives a more meaningful sense to MIMO efficiency. The input signal to all the ports (4)-ports in the proposed work) is the available power, transferred power is the radiation power and the difference between the two is the reflected power and thus, the square root ratio between the reflected power to that of the incident power is defined as $TARC_{MB}$ which is given by following Equations [41]

$$\Gamma_a^t = \frac{Available\ Power\ (AP) - Radiated\ Power\ (RP)}{Available\ Power\ (AP)} \tag{21}$$

For a lossless MIMO system with an N-number of elements or N-port, the $TARC_{MB}$ is given by

$$\Gamma_a^t = \frac{\sqrt{\sum_{i=1}^{N} |b_i|^2}}{\sqrt{\sum_{i=1}^{N} |a_i|^2}} \tag{22}$$

where [b]=[s][a]; a is the incident power with random phase and b is the reflected power.

In the propagation channel, the reflected signals are randomly phased because MIMO channels are assumed to be Gaussian and multipath spread propagation channels [41].

$$\begin{aligned} b_1 &= S_{11}a_1 + S_{12}a_2 = S_{11}a_0e^{j\theta_1} + S_{12}a_0e^{j\theta_2} \\ &= a_1\left(S_{11} + S_{12}e^{j\theta}\right) \end{aligned} \tag{23}$$

$$\begin{aligned} b_2 &= S_{21}a_1 + S_{22}a_2 = S_{21}a_0e^{j\theta_1} + S_{22}a_0e^{j\theta_2} \\ &= a_1\left(S_{21} + S_{22}e^{j\theta}\right) \end{aligned} \tag{24}$$

Combining Equations, $TARC_{MB}$

$$\Gamma_a^t = \frac{\sqrt{\left|S_{11} + S_{12}e^{j\theta}\right|^2 + \left|S_{21} + S_{22}e^{j\theta}\right|^2}}{\sqrt{2}} \tag{25}$$

Assuming $\theta = 0°$, $TARC_{MB}$ is evaluated from Equation 25 and is plotted in Fig. 9(e)-(f) for both simulated and measured S-parameters. The ideal values $TARC \leq 0dB$ and for the simulated and measured $TARC_{11}$, $TARC_{12}$, $TARC_{13}$, $TARC_{23}$, $TARC_{24}$, and $TARC_{34}$, the values are below −4.0dB.

The maximum transmission rate of the information over the channel with maximum limit is defined by Channel-Capacity-$Loss_{MB}$ (CCL_{MB}) with $CCL_{MB} \leq 0.40b/s/Hz$.

TABLE 3. Electrical property of phantom tissue.

Tissue	Permittivity (εr)	Conductivity (S/m)	Loss Tangent (tanδ)
Skin	38.8	1.18	0.30
Fat	5.30	0.07	0.14
Muscle	53.5	1.34	0.25

TABLE 4. SAR values at different frequency points.

Frequency (GHz)	Maximum SAR Value (W/Kg)	Maximum SAR (W/Kg)	Operating Bands (GHz)
11.0	0.366	<1.60	X-band
15.0	0.313		Ku band
20.0	0.424		K-band
24.0	0.418		5G-mmWave FR2 K-band
28.0	0.377		5G-mmWave FR2
30.0	0.309		Ka-band

The CCL_{MB} for a four-port MIMO antenna in generalized form is calculated by [41]

$$CCL_{60.0GHz} = -log_2 det\left(\alpha^s\right) \tag{26}$$

where

$$\rho_{mm} = 1 - \sum_{n=1}^{4} |S_{mn}|^2 \tag{27}$$

$$\rho_{ms} = -\left(S_{mm}^* S_{ms} + S_{sm}^* S_{ms}\right) \tag{28}$$

Fig 9. (g)-(h) shows the calculation of $CCL_{60.0GHz}$ for both simulated and measured reflection and transmission coefficients. The simulated averaged values $CCL_{MB} \leq 0.1b/s/Hz$ and measured averaged values correspond to $CCL_{MB} \leq 0.12b/s/Hz$.

The Mean-Effective-$Gain_{MB}$ (MEG_{MB}) is defined as the ratio of the received power to the power which will be received by an isotropic antenna when replaced [41].

In general, the MEG_{ms} are calculated by

$$MEG_{ms} = 0.5\left[1 - \sum_{s=1}^{K} |S_{ms}|^2\right] \tag{29}$$

$$MEG_m = 0.5 \times (1 - |S_{mm}|^2 - |S_{ms}|^2) \tag{30}$$

$$MEG_s = 0.5 \times (1 - |S_{ss}|^2 - |S_{sm}|^2) \tag{31}$$

The ratio calculates the $MEG_{60.0GHz}$ which is given by

$$\frac{MEG_m}{MEG_n} = \frac{0.5 \times (1 - |S_{mm}|^2 - |S_{mn}|^2)}{0.5 \times (1 - |S_{nn}|^2 - |S_{nm}|^2)} \tag{32}$$

For the $MEG_{\_port-m}$ and $MEG_{\_port-n}$ are evaluated from Equations (30) and Equation (31) with Equation (32) being the standard equation for MEG. Mean-Effective-$Gain_{60.0GHz}$ (MEG_{MB}) are evaluated between two-port as shown in

TABLE 5. State-of-the-art comparison.

Ref.	Size (λ_0^2)	Bandwidth (GHz)/%ge BW	Maximum Peak Gain (dBi)	No. of Rad. Elements	ECC	DG (dB)	TARC/ Isolation (dB)	CCL (b/s/Hz	MEG (dB)	SAR Value (W/Kg)	Conformal Capability	Potential Applications
[1]	$0.42\lambda_0\times0.71\lambda_0$	25.83-30.24 15.73%	4.00	1	NA	NA	NA	NA	NA	NA	No	mmWave
[2]	$2.14\lambda_0\times2.72\lambda_0$	26.52-29.50 16.22%	11.50	Array 1×4	NA	NA	NA	NA	NA	NA	No	mmWave
[4]	$3.00\lambda_0\times2.21\lambda_0$	45.0-62.5 28.0%	6.65	Array 2×2	NA	NA	NA	NA	NA	NA	No	mmWave
[6]	$0.15\lambda_0\times0.29\lambda_0$	2.26-2.73 13.20% 4.27-5.38 11.47%	7.18	1	NA	NA	NA	NA	NA	NA	No	ISM
[8]	$0.23\lambda_0\times0.39\lambda_0$	2.11-4.19 49.64% 4.98-6.81 26.87%	4.19	2	<0.004	>9.97	<-10.0 >21.0	<0.32	NA	NA	No	LTE Wi-Fi WLAN Bluetooth Wi-Max
[10]	$0.73\lambda_0\times1.21\lambda_0$	3.10-20.0 84.5%	NC	2	<0.15	>9.64	NC >20.0	NC	NC	NA	No	UWB X-band Ku-band
[17]	$0.47\lambda_0\times0.47\lambda_0$	2.97-15.48 74.15%	5.11	4	<0.20	>9.92	<-20.0 >16.0	<0.32	NC	NA	No	UWB X-band Ku-band
[18]	$1.20\lambda_0\times1.20\lambda_0$	3.18-11.50 72.35%	5.82	4	<0.005	>9.985	NC >16.0	<0.25	NC	NA	No	UWB X-band
[19]	$0.66\lambda_0\times0.66\lambda_0$	2.96-11.40 74.0%	4.85	4	<0.03	>9.982	<-12.0 >20.0	NC	NC	NA	No	UWB X-band
[20]	$0.21\lambda_0\times0.21\lambda_0$	1.15-40.0 97.13%	5.02	4	<0.005	NC	<-15.0 >25.0	NC	NC	NA	No	Bluetooth UWB X-band Ku-band K-band Ka-band
[21]	$3.89\lambda_0\times4.54\lambda_0$	25.5-29.6 13.85%	8.30	4	<0.02	>9.978	NC >30.0	<0.32	NC	NA	No	mmWave
[29]	$4.86\lambda_0\times6.11\lambda_0$	58.50	17.20	1	NA	NA	NA	NA	NA	NA	Yes	mmWave
[31]	$0.26\lambda_0\times0.29\lambda_0$	2.45 18.46%	0.50	2	<0.12	>9.85	NC >30.0	<0.08	NA	0.512	Yes	ISM
*P	$0.67\lambda_0\times0.67\lambda_0$	7.92-36.50 77.0%	7.17	4	<0.01	>9.996	<-4.0 >10.0	<0.38	≅0.0	0.366 at 11GHz 0.313 at 15GHz 0.424 at 20GHz 0.418 at 24GHz 0.377 at 28GHz 0.309 at 30GHz	Yes	X-band Ku-band K-band Ka-band FR2-mmWave

*P – Proposed work; NA-Not Applicable, NC-Not Calculated

Fig. 9(i)-(t). Fig. 9(i)-(k) corresponds to simulated MEG_{MB} for port1-port2, port1-port3 & port1-port4 and Fig. 9(l)-(n) corresponds to measured MEG_{MB} for port1-port2, port1-port3 & port1-port4. In both cases, the MEG_{MB} are nearly grazing -3.0dB values while the difference is nearly equal to 0.0dB. Similarly, MEG_{MB} for port2-port3, port2-port4 & port3-port4 also corresponds to −3.0dB in both simulated-Fig. 9(o)-(q) and measured results shown in Fig. 9(r)-(t).

Fig. 10 shows the simulated and measured peak gain & 2D-radiation pattern in principal planes. The peak gain is plotted in Fig. 10(a) which compares simulated and measured values for the operating bandwidth of 7.92GHz-36.50GHz and varies between 3.0dBi-7.02dBi with the highest peak corresponding to 8.28dBi at 26.875GHz for simulation and 4.50dBi-6.16dBi in measured environment with highest peak gain of 7.17dBi at 26.0GHz. For lower frequency points at 11.0GHz, 15.0GHz, and 20.0GHz, the 2D-radiation pattern corresponds to the desired dipole-omnidirectional pattern in both simulation-measured environments. However, at higher frequency points corresponding to 24.0GHz, 28.0GHz, and 30.0GHz, the 2D-radiation pattern does deviate from the ideal desired patterns but, is capable of transmitting and receiving the signals effectively when deployed in practical applications with wider-radiation patterns.

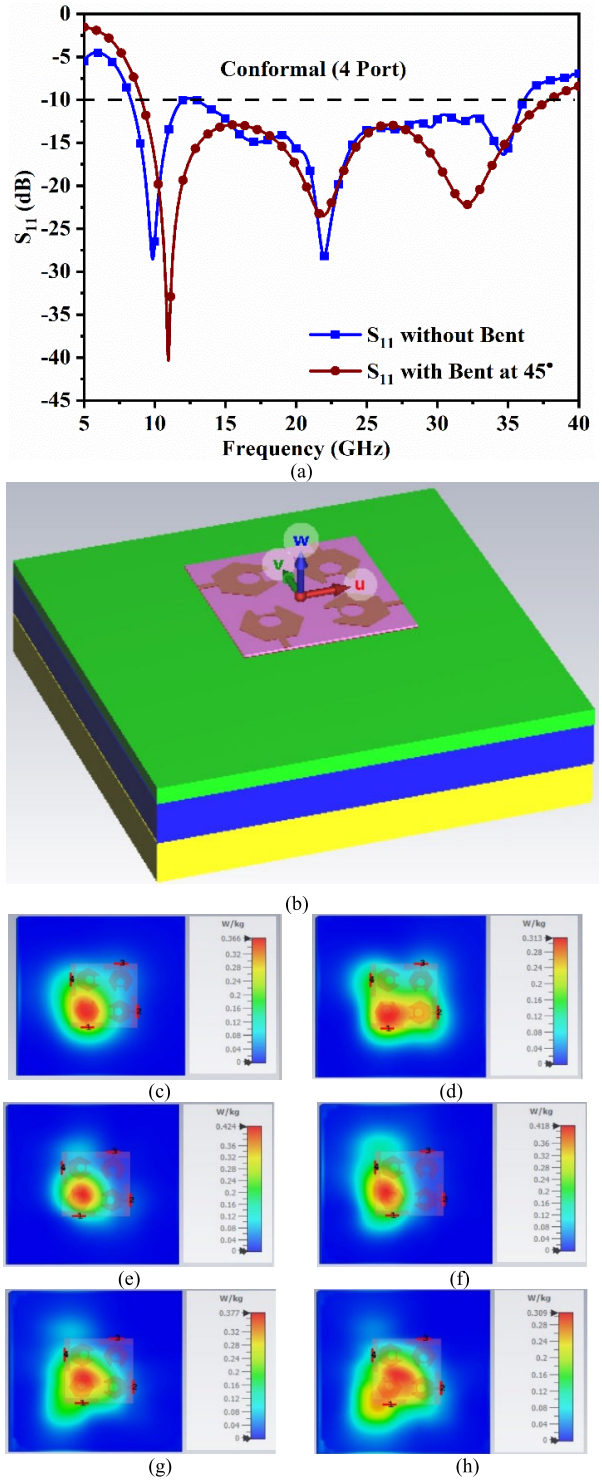

FIGURE 11. (a) S_{11} comparison of proposed MIMO antenna without bent and with bent at 45° (b) 3-D model of phantom tissue placed below radiating antenna; SAR at (c) 11.0GHz (d) 15.0GHz (e) 20.0GHz (f) 24.0GHz (g) 28.0GHz (h) 30.0GHz.

Fig. 10(i) shows the plot of simulated and measured radiation effeciency. The simulated radiation shows the variation between 89.44-95.94% whereas, the measured range lies between 88.96-94.32% and thus, confirms the good radiation characteristics of the proposed antenna in the working bandwidth of 8.31GHz-36.14GHz.

V. CONFORMAL CAPABILITY OF THE PROPOSED MIMO ANTENNA WITH SAR CALCULATION AND PRESENT STATE-OF-THE-ART MIMO ANTENNA COMPARISON

The proposed work utilizes a very thin substrate of thickness 0.254mm and hence, can be used in conformal applications. Due to the very compact size of the proposed MIMO antenna, it can be easily embedded within the devices designed for on-body applications with SAR within the specified limit.

The modeling of human tissue is utilized in calculating the Specific-Absorption-Rate (SAR) which signifies the amount of power absorbed by the human tissue when subjected to the interference of electromagnetic waves. The phantom layered of the human tissue consists of skin, fat, and muscle which represent the outermost layer of the body. This modeled human tissue is utilized to interact with the electromagnetic waves which are transmitted from the proposed MIMO antenna. The electrical properties which are already calculated [33] are assigned to all the layers of tissue for SAR analysis. The proposed MIMO antenna is placed on the assembled tissue layer with a gap of 5.00mm. The electrical parameters are tabulated in Table 3 given below

Fig. 11(a) shows the capability of the proposed four-port MIMO antenna with measured S_{11} parameter and corresponds to without and with conformal capability bent at 45°. From the observations, the S_{11} measures the bandwidth of 8.31GHz-36.14GHz without any bending and with bedding of 45° offers an impedance bandwidth of 9.05GHz-37.90GHz.

Fig. 11(b) shows the 3-D model of phantom tissue which is placed beneath the proposed MIMO configuration for SAR analysis and with a power input of 50 mW in CST-Microwave Studio EM-simulator. The three layers correspond to skin, fat, and muscle which forms the human tissue for the interaction of EM-wave radiated by the antenna to obtain SAR values for different frequency points specified within the operating bandwidth. The practical power absorbed by human tissue is defined by SAR when interacting with EM waves and is evaluated by [35]

$$SAR = \int \frac{\sigma\,(r)\,|E(r)|^2}{\rho(r)} dr \tag{33}$$

where σ-tissur conductivity (S/m), E is the electric field intensity (V/m) and ρ corresponds to tissue mass density (Kg/m3). For 1g of the tissue, the average SAR value must be less than 1.60 W/Kg [34]. Fig. 11(c)-(h) corresponds to the calculation of SAR for a wide range of frequencies and is given in Table 4

Table 5 shows a brief comparison of the proposed four-port MIMO antenna with the present state-of-the-art. It can be noted that the proposed MIMO antenna offers wider impedance bandwidth fabricated on a very thin substrate which is utilized for conformal applications. Also, for on-body applications, the antenna is analyzed for

SAR applications which are calculated at different frequency points and include different band applications. All the above features outclass the other published work which are compared in Table 5.

VI. CONCLUSION

A four-port MIMO antenna with conformal capability and SAR analysis is presented. The proposed MIMO antenna occupies wider impedance bandwidth which includes applications in Microwave-Millimeter wave bands including X-band, Ku-band, K-band, partial Ka-band, n257, n258, and n261 bands. The proposed MIMO antenna offers a measured averaged peak gain of 5.50dBi and 2D-dipole-omnidirectional patterns. The MIMO antenna is also evaluated with group delay and impulse response. The diversity parameters are well within the permissible values. The SAR analysis of the MIMO antenna is less than 1.60W/Kg in the frequency values within the operating bandwidth.

REFERENCES

[1] P. Kumar, T. Ali, O. P. Kumar, S. Vincent, P. Kumar, Y. Nanjappa, and S. Pathan, "An ultra-compact 28 GHz arc-shaped millimeter-wave antenna for 5G application," *Micromachines*, vol. 14, no. 1, p. 5, Dec. 2022.

[2] S. H. Kiani, X. C. Ren, A. Bashir, A. Rafiq, and M. R. Anjum, "Square-framed *T* shape mmWave antenna array at 28 GHz for future 5G devices," *Int. J. Antennas Propag.*, vol. 2021, Sep. 2021, Art. no. 2286011.

[3] M. H. Sharaf, A. I. Zaki, R. K. Hamad, and M. M. M. Omar, "A novel dual-band (38/60 GHz) patch antenna for 5G mobile handsets," *Sensors*, vol. 20, no. 9, p. 2541, Apr. 2020.

[4] A. G. Alharbi, H. M. A. Rahman, M. M. Khan, M. I. Abbasi, A. A. Albraikan, and F. A. Almalki, "Design and study of a miniaturized millimeter wave array antenna for wireless body area network," *Int. J. Antennas Propag.*, vol. 2022, pp. 1–25, May 2022.

[5] A. Dejen, J. Jayasinghe, M. Ridwan, and J. Anguera, "Synthesis of quad-band mm-Wave microstrip antenna using genetic algorithm for wireless application," *Technologies*, vol. 11, no. 1, p. 14, Jan. 2023.

[6] A. Gupta, A. Kansal, and P. Chawla, "Design of a compact dual-band antenna for on-/off body communication," *IETE J. Res.*, vol. 69, no. 2, pp. 1013–1021, Feb. 2020.

[7] M. Sharma, "Superwideband triple notch monopole antenna for multiple wireless applications," *Wireless Pers. Commun.*, vol. 104, no. 1, pp. 459–470, Jan. 2019.

[8] R. N. Tiwari, P. Singh, B. K. Kanaujia, S. Kumar, and S. K. Gupta, "A low profile dual band MIMO antenna for LTE/Bluetooth/Wi-Fi/WLAN applications," *J. Electromagn. Waves Appl.*, vol. 34, no. 9, pp. 1239–1253, Jun. 2020.

[9] H. Ullah, H. F. Abutarboush, A. Rashid, and F. A. Tahir, "A compact low-profile antenna for millimeter-wave 5G mobile phones," *Electronics*, vol. 11, no. 19, p. 3256, Oct. 2022.

[10] B. T. Ahmed, P. S. Olivares, J. L. M. Campos, and F. M. Vázquez, "(3.1–20) GHz MIMO antennas," *AEU Int. J. Electron. Commun.*, vol. 94, pp. 348–358, Sep. 2018.

[11] J. Khan, S. Ullah, U. Ali, F. A. Tahir, I. Peter, and L. Matekovits, "Design of a millimeter-wave MIMO antenna array for 5G communication terminals," *Sensors*, vol. 22, no. 7, p. 2768, Apr. 2022.

[12] H. Ekrami and S. Jam, "A compact triple-band dual-element MIMO antenna with high port-to-port isolation for wireless applications," *AEU Int. J. Electron. Commun.*, vol. 96, pp. 219–227, Nov. 2018.

[13] Z. Li, C. Yin, and X. Zhu, "Compact UWB MIMO Vivaldi antenna with dual band-notched characteristics," *IEEE Access*, vol. 7, pp. 38696–38701, 2019.

[14] Z. Tang, J. Zhan, X. Wu, Z. Xi, L. Chen, and S. Hu, "Design of a compact UWB-MIMO antenna with high isolation and dual band-notched characteristics," *J. Electromagn. Waves Appl.*, vol. 34, no. 4, pp. 500–513, Mar. 2020.

[15] S. Tariq, S. I. Naqvi, N. Hussain, and Y. Amin, "A metasurface-based MIMO antenna for 5G millimeter-wave applications," *IEEE Access*, vol. 9, pp. 51805–51817, 2021.

[16] T. Addepalli, T. Vidyavathi, K. Neelima, M. Sharma, and D. Kumar, "Asymmetrical fed Calendula flower-shaped four-port 5G-NR band (n77, n78, and n79) MIMO antenna with high diversity performance," *Int. J. Microw. Wireless Technol.*, vol. 15, pp. 1–15, Jul. 2022.

[17] M. Sharma, V. Janghu, and N. Kumar, "Dual notched four-port multiband reconfigurable MIMO antenna with novel fork-radiator and Ω-shaped ground," *IETE J. Res.*, pp. 1–14, Aug. 2022.

[18] M. N. Hasan, S. Chu, and S. Bashir, "A DGS monopole antenna loaded with U-shape stub for UWB MIMO applications," *Microw. Opt. Technol. Lett.*, vol. 61, no. 9, pp. 2141–2149, Sep. 2019.

[19] A. Mchbal, N. Amar Touhami, H. Elftouh, and A. Dkiouak, "Coupling reduction using a novel circular ripple-shaped decoupling mechanism in a four-element UWB MIMO antenna design," *J. Electromagn. Waves Appl.*, vol. 34, no. 12, pp. 1647–1666, Aug. 2020.

[20] D. Kumar Raheja, S. Kumar, B. Kumar Kanaujia, S. Kumar Palaniswamy, R. Rao Thipparaju, and M. Kanagasabai, "Truncated elliptical self-complementary antenna with quad-band notches for SWB MIMO systems," *AEU Int. J. Electron. Commun.*, vol. 131, Mar. 2021, Art. no. 153608.

[21] M. Khalid, S. I. Naqvi, N. Hussain, M. Rahman, S. S. Mirjavadi, M. J. Khan, and Y. Amin, "4-port MIMO antenna with defected ground structure for 5G millimeter wave applications," *Electronics*, vol. 9, no. 1, p. 71, Jan. 2020.

[22] K. Raheel, A. Altaf, A. Waheed, S. H. Kiani, D. A. Sehrai, F. Tubbal, and R. Raad, "E-shaped H-slotted dual band mmWave antenna for 5G technology," *Electronics*, vol. 10, no. 9, p. 1019, Apr. 2021.

[23] S. Juneja, R. Pratap, and R. Sharma, "Semiconductor technologies for 5G implementation at millimeter wave frequencies–design challenges and current state of work," *Eng. Sci. Technol., Int. J.*, vol. 24, no. 1, pp. 205–217, Feb. 2021.

[24] E. Al Abbas, M. Ikram, A. T. Mobashsher, and A. Abbosh, "MIMO antenna system for multi-band millimeter-wave 5G and wideband 4G mobile communications," *IEEE Access*, vol. 7, pp. 181916–181923, 2019.

[25] T. Addepalli, J. Babu Kamili, K. Kumar Bandi, A. Nella, and M. Sharma, "Lotus flower-shaped 4/8-element MIMO antenna for 5G n77 and n78 band applications," *J. Electromagn. Waves Appl.*, vol. 36, no. 10, pp. 1404–1422, Jul. 2022.

[26] T. Addepalli, M. Sharma, A. Nella, A. P. Ambalgi, and P. R. Kapula, "Experimental investigation of super-wideband 8-port multiple-input-multiple-output antenna with high isolation for future wireless applications including Internet of Things," *Int. J. Commun. Syst.*, p. e5199, May 2022.

[27] G. Kumar and R. Kumar, "A survey on planar ultra-wideband antennas with band notch characteristics: Principle, design, and applications," *AEU Int. J. Electron. Commun.*, vol. 109, pp. 76–98, Sep. 2019.

[28] P. Gupta, L. Malviya, and S. V. Charhate, "5G multi-element/port antenna design for wireless applications: A review," *Int. J. Microw. Wireless Technol.*, vol. 11, no. 9, pp. 918–938, Nov. 2019.

[29] V. Semkin, A. Bisognin, M. Kyrö, V.-M. Kolmonen, C. Luxey, F. Ferrero, F. Devillers, and A. V. Räisänen, "Conformal antenna array for millimeter-wave communications: Performance evaluation," *Int. J. Microw. Wireless Technol.*, vol. 9, no. 1, pp. 241–247, Feb. 2017.

[30] D. Negi, R. Khanna, and J. Kaur, "Design and performance analysis of a conformal CPW fed wideband antenna with mu-negative metamaterial for wearable applications," *Int. J. Microw. Wireless Technol.*, vol. 11, no. 8, pp. 806–820, Oct. 2019.

[31] A. Gupta, A. Kansal, and P. Chawla, "Design of a wearable MIMO antenna deployed with an inverted U-shaped ground stub for diversity performance enhancement," *Int. J. Microw. Wireless Technol.*, vol. 13, no. 1, pp. 76–86, Feb. 2021.

[32] A. Gupta, P. Chawla, A. Kansal, and K. Singh, "An active and low-cost microwave imaging system for detection of breast cancer using back scattered signal," *Current Med. Imag. Formerly Current Med. Imag. Rev.*, vol. 18, no. 5, pp. 460–475, May 2022.

[33] A. Gupta, A. Kansal, and P. Chawla, "Design of a patch antenna with square ring-shaped-coupled ground for on-/off body communication," *Int. J. Electron.*, vol. 106, no. 12, pp. 1814–1828, Dec. 2019.

[34] A. Gupta, A. Kansal, and P. Chawla, "A survey and classification on applications of antenna in health care domain: Data transmission, diagnosis and treatment," *Sādhanā*, vol. 46, no. 2, p. 68, Jun. 2021.

[35] V. Karthik and T. Rama Rao, "Investigations on SAR and thermal effects of a body wearable microstrip antenna," *Wireless Pers. Commun.*, vol. 96, no. 3, pp. 3385–3401, Oct. 2017.

[36] A. Kumar, S. Sharma, N. Goyal, A. Singh, X. Cheng, and P. Singh, "Secure and energy-efficient smart building architecture with emerging technology IoT," *Comput. Commun.*, vol. 176, pp. 207–217, Aug. 2021.
[37] K. Liu, Z. Li, W. Cui, K. Zhang, M. Wang, C. Fan, H. Zheng, and E. Li, "Investigation of conformal MIMO antenna for implantable devices based on theory of characteristic modes," *IEEE Trans. Antennas Propag.*, vol. 70, no. 12, pp. 11324–11334, Dec. 2022, doi: 10.1109/TAP.2022.3209236.
[38] G. Das, A. Sharma, R. K. Gangwar, and M. S. Sharawi, "Performance improvement of multiband MIMO dielectric resonator antenna system with a partially reflecting surface," *IEEE Antennas Wireless Propag. Lett.*, vol. 18, no. 10, pp. 2105–2109, Oct. 2019, doi: 10.1109/LAWP.2019.2938004.
[39] G. Das, N. K. Sahu, A. Sharma, R. K. Gangwar, and M. S. Sharawi, "FSS-based spatially decoupled back-to-back four-port MIMO DRA with multidirectional pattern diversity," *IEEE Antennas Wireless Propag. Lett.*, vol. 18, no. 8, pp. 1552–1556, Aug. 2019, doi: 10.1109/LAWP.2019.2922276.
[40] M. Sharma, Y. K. Awasthi, H. Singh, R. Kumar, and S. Kumari, "Compact printed high rejection triple band-notch UWB antenna with multiple wireless applications," *Eng. Sci. Technol., Int. J.*, vol. 19, no. 3, pp. 1626–1634, Sep. 2016.
[41] M. Sharma, P. C. Vashist, P. S. Ashtankar, and S. K. Mittal, "Compact 2 × 2/4 × 4 tapered microstrip feed MIMO antenna configuration for high-speed wireless applications with band stop filters," *Int. J. RF Microw. Comput.-Aided Eng.*, vol. 31, no. 1, pp. 1–16, Jan. 2021.

MANISH SHARMA (Senior Member, IEEE) received the B.E. degree in electronics and communication engineering from Mangalore University, Karnataka, India, in 2000, the M.Tech. degree from Visvesvaraya Technological University, Karnataka, in 2007, and the Ph.D. degree from the Department of Electronics Engineering, Banasthali University, Rajasthan, India, in 2017. He is currently a Professor and a Researcher with the Chitkara University Research and Innovation Network (CURIN), Chitkara University, Punjab, India. He is also the Director of Spectrum Wirelesscomm Pvt., Ltd., which provides solutions in healthcare and agricultural problems. He has published more than 100 research articles and granted eight patents. He is currently guiding eight Ph.D. students. He has also published 18 book chapters. His current research interests include computational electromagnetics, reconfigurable antennas, novel electromagnetic materials, dielectric resonator antennas, wideband/super-wideband antennas, wideband/dual band/triple band microstrip antennas for wireless communication, smart and MIMO antenna systems, radio-frequency identification (RFID) antennas, antennas for healthcare, RF MEMS planar antenna on Si substrate, wireless networks, body area networks, meta surface-based biosensors, and the designing of microstrip antennas using machine learning and artificial networks. He is also a Reviewer of IEEE Access, *Journal of Electromagnetic Waves and Applications*, *International Journal of Electronics and Communication* (AEU), *International Journal of Communication Systems*, *International Journal of Microwave and Wireless Technologies*, and *International Journal of RF and Microwave Computer-Aided Engineering*.

PRABHAKARA RAO KAPULA (Member, IEEE) received the B.E. degree in electronics and communication engineering from Andhra University, in 1996, the M.Tech. degree in instrumentation and control systems from the JNTU College of Engineering, Hyderabad, and the Ph.D. degree from Andhra University. He has 24 years of teaching experience. He is currently a Professor with the Department of Electronics and Communication Engineering, B. V. Raju Institute of Technology, Narsapur, Telangana. He is also working on a DST-TIDE research project on a paraplegic patient's mobility assistance device. His current research interests include wireless communication, MIMO antennas, biosensors, and medical assistive technology. In addition to being awarded one patent, he has more than 50 research publications published in various journals with SCI, SCOPUS, and WoS indexes. He reviews articles for *International Journal of Wireless Information Networks* and IEEE Transactions on Signal Processing. He is a fellow of IETE.

SHAILAJA SALAGRAMA (Member, IEEE) received the M.S. degree from Chicago State University, in 2017. She is currently pursuing the Ph.D. degree with the University of the Cumberland, KY, USA. She was a Network Administrator with Accenture. She was an Assistant Professor with Indian University, for more than four years of teaching experience. Her current research interests include the IoT, 5G, wireless networks, body area networks, and machine learning.

KANHAIYA SHARMA (Member, IEEE) received the M.Tech. degree in computer science and engineering from Jawaharlal Lal Technological University, Hyderabad, India, in 2011, and the Ph.D. degree in computer science and engineering from Pandit Deendayal Energy University, Gandhinagar, Gujarat, India, in 2021. From 2010 to 2017, he was an Assistant Professor with the Siddhant Group of Institution, Sudumbare, Pune, Maharashtra, India. From 2020 to 2021, he was an Assistant Professor with the Computer Science and Engineering Department, Sandip University, Nashik, Maharashtra. From August 2021 to July 2022, he was an Assistant Professor with the Computer Science and Engineering Department, Anurag University, Hyderabad, Telangana, India. He is currently an Assistant Professor with the Department of Computer Science and Engineering, Symbiosis Institute of Technology, Symbiosis International University, Lavale, Pune. He has authored or coauthored several journals and IEEE proceeding publications. His current research interests include the next generation of mm-wave and the development of low-cost solutions for wireless applications, machine learning, wireless communications, microstrip antenna design, filter design, and artificial intelligence. He is an active reviewer for many reputed IEEE journals and letters.

GANGA PRASAD PANDEY (Senior Member, IEEE) received the B.Tech. degree in electronics and communication engineering from KNIT Sultanpur, Uttar Pradesh, in 2000, the M.E. degree from the Delhi College of Engineering, Delhi, India, in 2004, and the Ph.D. degree in tunable microstrip antenna from Uttarakhand Technical University, Dehradun, U.K., in 2015. He has more than 21 years of teaching experience. Currently, he is heading the Department of Information and Communication Technology, Pandit Deendayal Energy University, Gandhinagar. He has published more than 40 articles in international journals of repute and more than 20 papers in international conferences. He has guided four Ph.D. scholars in the domain of antennas. His current research interests include energy harvesting, ME-dipole, active, reconfigurable, frequency agile microstrip antennas, and microwave/millimeter wave integrated circuits and devices.

DINESH KUMAR SINGH received the B.E. degree in electronics and communication engineering from the Kumaon Engineering College, Dwarahat, Almora, in 2003, the M.Tech. degree in digital communication from RGPV University, Bhopal, India, and the Ph.D. degree from the Indian Institute of Technology (ISM), Dhanbad, Jharkhand, India. He is currently a Professor with the Electronics and Communication Engineering Department, GL Bajaj Institute of Technology and Management, Greater Noida, Uttar Pradesh, India. He has been credited with publishing more than 20 papers in various reputed international journals and conferences. His current research interests include microwave engineering, the designing of high-gain, compact, re-configurable, fractal-shape, circularly polarized microstrip antennas, substrate integrated waveguide (SIW), and magneto-electric (ME) dipole antenna for modern communication systems. He is a Reviewer of the *International Journal of Electronics and Communication* (AEU) and *Electronics Letter*.

MILIND MAHAJAN (Senior Member, IEEE) received the B.E. degree in electronics from Marathwada University, in 1991, the M.Tech. degree in microwave engineering from IITBHU, in 1993, and the Ph.D. degree from Dharmsinh Desai University, Nadiad, in 2015. In 1993, he started his career with the Spacecraft Payload Group, Space Applications Centre, Ahmedabad. He was a Guest Scientist with the German Aerospace Centre (DLR), in 2001. He is currently the Group Director of the Antenna Systems Group at Space Application Center, ISRO, Ahmedabad, GJ, India. He has more than 50 publications in national/international journals and conferences and three patents to his credit. His current research interests include contoured beam reflectors and digital beamforming antennas. He has led the team to develop the antenna systems for navigation, radar imaging, communication satellites (like INSAT-4A/4B/4C, GSAT-7/7A, and GSAT-11), and the Chandrayaan-2 mission. He was a recipient of the Space Gold Medal of the Astronautical Society of India, in 2005, and the ISRO's Team Excellence Awards, in 2007, 2008, 2015, and 2017.

ANUPMA GUPTA received the B.E. degree in electronics and communication engineering from Guru Jambheshwar University, Haryana, India, in 2006, the M.Tech. degree from Maharishi Markandeshwar University, Haryana, in 2010, and the Ph.D. degree from the Department of Electronics Engineering, Thapar Institute of Engineering and Technology, Punjab, India, in 2021. She is currently an Assistant Professor with Chitkara University, Punjab. She has published more than 25 research articles and granted four patents. Her current research interests include computational electromagnetics, reconfigurable antennas, novel electromagnetic materials, dielectric resonator antennas, wideband/superwide band antennas, wideband/dual band/triple band microstrip antennas for wireless communication, smart and MIMO antenna systems, antennas for healthcare, and RF MEMS planar antenna. She is a reviewer of various reputed journals.